nature
structural &
molecular biology

Pore-opening mechanism of the nicotinic acetylcholine receptor evinced by proton transfer

Gisela D Cymes & Claudio Grosman

The conformational changes underlying cysteine-loop receptor channel gating remain elusive and controversial. We previously developed a single-channel electrophysiological method that allows structural inferences about the transient open-channel conformation to be made from the effect and properties of introduced charges on systematically engineered ionizable amino acids. Here we have applied this methodology to the entire M1 and M3 segments of the muscle nicotinic acetylcholine receptor, two transmembrane α-helices that pack against the pore-lining M2 α-helix. Together with our previous results on M2, these data suggest that the pore dilation that underlies channel opening involves only a subtle rearrangement of these three transmembrane helices. Such a limited conformational change seems optimal to allow rapid closed-open interconversion rates, and hence a fast post-synaptic response upon neurotransmitter binding. Thus, this receptor-channel seems to have evolved to take full advantage of the steep dependence of ion- and water-conduction rates on pore diameter that is characteristic of model hydrophobic nanopores.

Various approaches have contributed to the development of a structural model of the closed-channel conformation of the muscle-type nicotinic acetylcholine receptor[1] (AChR), an archetypal member of the cysteine-loop receptor superfamily of pentameric neurotransmitter-gated ion channels (**Fig. 1**). At the level of the membrane, 20 helices (4 per subunit) are arranged in concentric layers around a central aqueous pore, with M2 directly lining the cation-selective permeation pathway, M1 and M3 shielding M2 from the surrounding lipid bilayer and M4 being the outermost and most lipid-exposed segment. Although some uncertainty remains as to the exact positioning of the side chains, it seems clear that this model is, otherwise, essentially correct.

Less is known, however, about the open-channel conformation. Because, on exposure to saturating concentrations of acetylcholine (ACh), closed AChRs open only to shut ('desensitize') again with an ~50-ms time constant (ref. 2), the structure of the open conformation (and therefore the molecular basis of cysteine-loop receptor-channel gating) has remained largely elusive. And, although freeze-trapping experiments probably succeed in isolating the open state of the receptor (upon fast application of high concentrations of agonist), important limitations remain. For example, cryo-EM images from freeze-trapped open AChRs suggested that the pore expands upon opening[3], but the low resolution of the data (9 Å) precludes a description of the geometrical properties of the transmembrane α-helices in the open channel. Photoaffinity labeling of trapped-open receptors also suggested conformational rearrangements of the pore domain upon opening, in this case leading to the formation of a hydrophobic pocket (large enough to fit a diazirine-based photoreactive probe) contralateral to the pore and lined by the extracellular ends of the M1, M2 and M3 segments of the AChR's δ subunit[4]. However, the relatively large size of the probe (~11×7×7 Å), along with the need to limit the incubation times with agonist to only a few milliseconds to minimize desensitization (too short a time period for the photolabel to equilibrate with the open conformation), necessarily limits the structural information that can be gained from this approach. On the other hand, labeling studies that do not involve some type of isolation of the open conformation face the problem that (at the low concentrations of agonist typically used) the open state coexists with the closed and desensitized forms of the receptor, and hence ascribing the label to a particular state in the mixture may be difficult.

Despite these limitations, various molecular rearrangements have been proposed to underlie AChR gating. These range from large (~180°)[5] to small (~15°)[6,7] rotations of M2 about an axis normal to the bilayer, and from small changes in tilt angle about a pivot point located in the intracellular half of M2 (ref. 8) to larger tilting motions about a fulcrum in the extracellular half of M2 (ref. 9). Moreover, a recent series of molecular simulation studies, aimed at elucidating the initial rearrangements leading from the closed to the open state of the AChR, have made it clear that not only is the relatively short duration of the simulations an important caveat, but also that the results are highly sensitive to the details of the structural model under consideration[7,9,10]. This is unfortunate, because atomic-resolution data from the AChR's transmembrane domain in the closed conformation (let alone in the open conformation) are still unavailable.

There is no doubt that the AChR's transmembrane segments must rearrange themselves during gating. In addition to the obvious need for the closed-channel 'gate' to be removed upon opening, the often profound effect of pore mutations on the closed open-equilibrium constant is a compelling example of the large amount of experimental

Department of Molecular and Integrative Physiology, Center for Biophysics and Computational Biology and Neuroscience Program, University of Illinois at Urbana-Champaign, 407 South Goodwin Avenue, 524 Burrill Hall, Urbana, Illinois 61801, USA. Correspondence should be addressed to C.G. (grosman@life.uiuc.edu).

Received 19 November 2007; accepted 25 February 2008; published online 30 March 2008; doi:10.1038/nsmb.1407

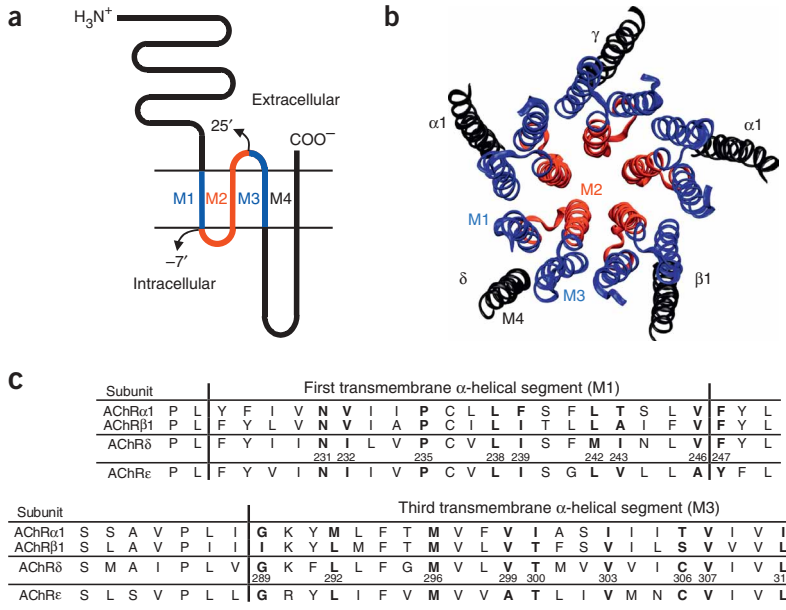

Figure 1 General properties of the AChR. (**a**) Membrane-threading pattern common to all cysteine-loop receptors, a superfamily of ligand-gated ion channels that, in vertebrates, includes receptors to acetylcholine, serotonin, γ-amino-butyric acid and glycine. The portion of the transmembrane domain studied in this paper is denoted in blue; in red is the region studied in our previous work[11]. (**b**) Ribbon representation of the transmembrane portion of the PDB file 2BG9 (ref. 1), a model of *Torpedo*'s electric-organ AChR (a muscle-type AChR) in the closed state, as viewed from the extracellular side. The color code is the same as in **a**. In adult muscle, the γ subunit is replaced by the ε subunit. The molecular image was made with VMD[46]. (**c**) Sequence alignment of the 57 positions studied here. The four adult mouse muscle AChR subunits (α1, β1, δ and ε) are compared. Vertical lines indicate the approximate ends of the α-helical stretches, largely as suggested by analysis of the PDB file 2BG9 with the program STRIDE[47]. Positions that, according to our data, are oriented toward the lumen of the open-channel pore are indicated in bold for the four subunits.

evidence for this idea. What the estimation of gating $\Delta\Delta G^\circ$ values cannot easily address, however, is the extent to which the structure of the pore domain changes during this conformational change. This is precisely the gap this paper seeks to fill.

To gain insight into the structural properties of the AChR's transmembrane segments in the open conformation, we applied a recently developed single-channel proton-transfer technique[11]. Because identification of the open state in a single-channel current recording is unequivocal, our approach circumvents the problems associated with the transient and short-lived nature of the open conformation altogether. In this electrophysiological approach, lysines, arginines or histidines are systematically introduced at different positions in the protein to probe both the proximity of the mutated position to the pore's long axis (as judged from the extent to which the cation currents are attenuated, or 'blocked', upon side-chain protonation) and the degree of side-chain solvation by water molecules and the rest of the protein (as judged from the side-chain pK_a-shifts relative to bulk water). The results from our previous application of this approach to the pore-lining M2 α-helices[11] strongly suggest that, however complex the physicochemical principles underlying the observed phenomena, the interpretation of these two observables is straightforward: the larger the extent of block, the closer the engineered ionizable side chain to the pore's long axis and the more downshifted the pK_a value, the poorer the positive-charge stabilizing properties of the side chain's microenvironment compared to those of bulk water[12–19]. Given that, in the AChR's transmembrane region, naturally occurring ionizable residues are confined to the ends of the membrane-embedded segments, the observed changes in pK_a values are expected to reflect (at most mutated positions) the interactions of the engineered positive charges with water molecules and dipolar groups in the protein (that is, backbone dipoles and polar side chains) rather than interactions with other protein charges. As our results below suggest, the recorded gradients of ΔpK_a values seem to report, specifically, on the distribution of water molecules around the transmembrane segments of the AChR.

Application of this new methodology to the pore-lining M2 segments of the mouse muscle AChR led us to conclude that there is minimal, if any, rotation of these α-helices (about an axis normal to the bilayer) upon channel opening[11]. Here we set out to apply this approach to M1 and M3, the two transmembrane segments that, along with M2, make the most extensive contacts with the (extracellular) neurotransmitter binding domain[1].

RESULTS

A closer look at the closed state

Upon quantitative inspection of the closed-channel structural model (PDB file 2BG9)[1], we generated the plot in **Figure 2a**. This plot clearly suggests the identity of the positions in M1 and M3 that are closest to the pore's lumen and reveals that the helical axis of M1 is closer to the long axis of the pore than is that of M3, for most of its length. Further examination of the structural model indicates that the reason why the Cα trace of M1 approaches the lumen more closely is not because the interaxial distance between M1 and M2 (of the same subunit) is shorter than that between M3 and M2 (actually, they are almost identical; **Supplementary Fig. 1** online) but because the arrangement of these three α-helices in the membrane is such that M1 packs against the groove formed by two adjacent M2 helices whereas M3 packs against the back side of the M2 helix in the same subunit (**Fig. 2b,c**). This brings the M1 segments closer not only to the pore's long axis, but also to the lateral stripes of M2.

From the observations above, several predictions can be made. First, if M1 did not rotate upon channel opening, then the same M1 positions that are oriented toward the pore (hereafter the 'front stripe' of M1) in the closed state should be the ones exerting the most open-channel block when mutated to basic residues; of course, the same is expected in the case of M3. Second, if (upon channel opening) the helical axis of M1 remained closer to the pore's long axis than did the helical axis of M3, then the extent of channel block caused by basic side chains engineered on the front stripe of M1 should be larger than that corresponding to M3. And, third, if the rearrangement of the M1–M2 and M3–M2 packing interfaces that takes place upon channel opening (for example, refs. 4,20) did not involve large displacements of these three helices relative to each other, then the long side chains of lysines and arginines engineered on the front stripe of M1 should block the currents nearly as much as those on the lateral stripes of M2 (that is, less than those on the front of M2 but more than those on its back). Similarly, the extent of block exerted by these long side chains

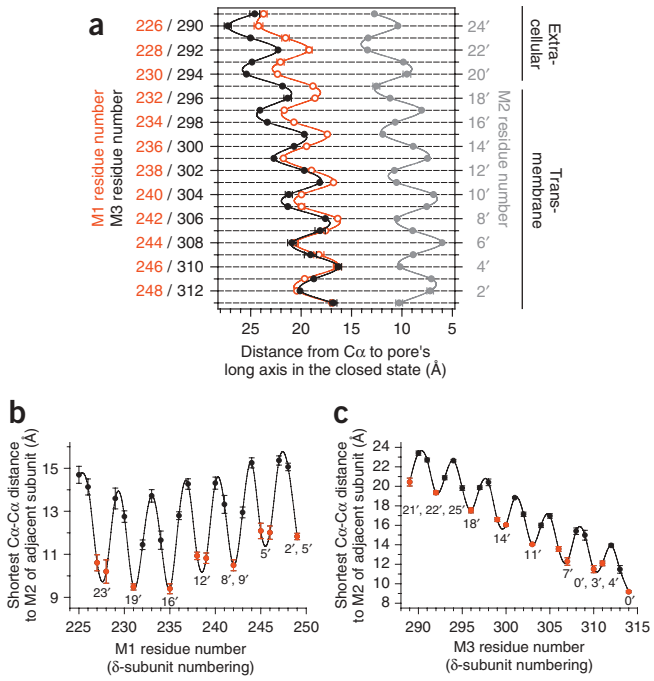

Figure 2 Geometrical relationships between M1, M2, M3 and the pore in the closed state. (**a**) Distances from the Cα atoms to the long axis of the pore measured for M1 (open red circles), M2 (filled gray circles) and M3 (filled black circles). M1 and M3 residue numbers (in red and black, respectively) correspond to those of the δ subunit. M2 positions are denoted using the prime-numbering system (see **Figure 1a**), which assigns positions α1Lys242, β1Lys253, δLys256 and εLys252 to 0′. (**b**) All possible Cα–Cα distances between the M1 segment of each subunit and the M2 segment of the subunit to the left, as seen from the extracellular side (**Fig. 1b**), were measured, and the shortest ones are plotted as a function of M1 residue number. The minima (indicated in red) identify the interfacial positions in M1. The interfacial positions in the (adjacent-subunit) M2 segment vary among subunits and are indicated next to these minima using the prime-numbering system. The mean value of the minima (that is, the mean Cα–Cα distance at the interface) is 10.8 Å ± 0.3 Å. (**c**) The mean Cα–Cα distance at the M3–M2 interface is 14.8 Å ± 1.1 Å. In this case, the 'adjacent subunit' is the subunit to the right (that is, the one to which M3 is closest), as seen from the extracellular side (**Fig. 1b**). It is clear that M1 is closer to the adjacent subunit's M2 segment than M3 is. Means and standard errors were calculated from the values corresponding to the five individual subunits, and the unbroken lines are cubic-spline interpolations. All distances were measured on the PDB file 2BG9 (ref. 1) using VMD[46].

on the front of M3 should be comparable to that caused by these side chains on the back side of M2.

Testing predictions

To test the predictions above, each position of the M1 and M3 segments, and part of the M2–M3 linker of the mouse muscle AChR δ subunit, were mutated (one at a time) to lysine (**Fig. 1c**), and single-channel currents were recorded (**Fig. 3**; together with our previous work[11], this mutagenesis completes the introduction of basic residues from the first position in M1 through the last one in M3). With only a few exceptions, all lysine substitutions resulted in functional AChRs. The exceptions are lysine substitutions at the positions occupied by residues Pro235, Val246 and Phe247, all in δM1, Pro286 in the δM2–M3 linker and Val307 in δM3. However, the three M1 mutations did result in functional channels when engineered at the aligned positions in the β1 subunit (that is, Pro232, Val243 and Phe244). In contrast, the mutations in the M2–M3 linker and M3 also failed to yield functional channels at the aligned β1 subunit positions (that is, Pro283 and Val304). Hence, these are the only two sites (out of a total of 89 tested, including the 32 positions mutated in M2) for which we could not obtain any information as to the magnitude of their current-blocking effect or their ΔpK_a values.

We estimated the extent of channel block corresponding to M1 and M3, and plotted these values together with data for M2 (**Fig. 4**) to allow for a direct comparison with **Figure 2a**. Whereas the latter figure plots actual distances between Cα atoms and the long axis of the pore in the closed-channel structural model (PDB file 2BG9)[1], **Figure 4b** plots a quantity that depends on the distance between the engineered protonatable groups (located some ångströms away from the Cα atoms to which they are 'tethered') and the pore's long axis in the open state. At many positions, both in M1 and M3, engineered lysines or arginines fail to block the currents, even at pH 6.0. For at least some of the positions that protrude from the lipid bilayer into the intra- or extracellular space, this lack of effect on the currents could be due to the side chains being solvated by water molecules with bulk-like properties, in such a way that the electrostatic effect of the positively charged side chains is completely screened. For the membrane-embedded positions, on the other hand, the absence of blocking may indicate that the side chains are located too far from the pore's long axis (such that protonation-deprotonation events of the ionizable groups would go undetected, even if they occurred) and/or that the side chains are so poorly solvated by their surroundings that protonation becomes extremely unlikely.

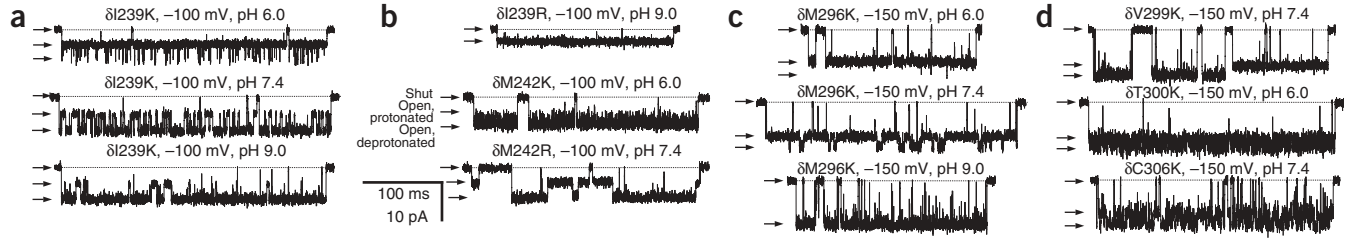

Figure 3 pH- and position-dependence of proton-transfer events. Individual protonation-deprotonation reactions of basic residues in cation-selective channels may manifest in single-channel patch-clamp recordings as fluctuations of the cation current between two levels of different conductance: a wild type–like level (corresponding to the neutral, deprotonated side chain) and a level of lower conductance (corresponding to the positively charged, protonated side chain). Arrows indicate the shut (zero current) and the two open-channel current levels. The shut level of each trace is also indicated by a horizontal broken line. Display f_c = 6 kHz. [ACh] = 1 μM. Example single-channel inward currents recorded from four M1 (**a**,**b**) and four M3 (**c**,**d**) mutants. The transmembrane potential in **c** and **d** is more hyperpolarized than that in **a** or **b** to allow a better appreciation of the difference between the two open-channel current levels.

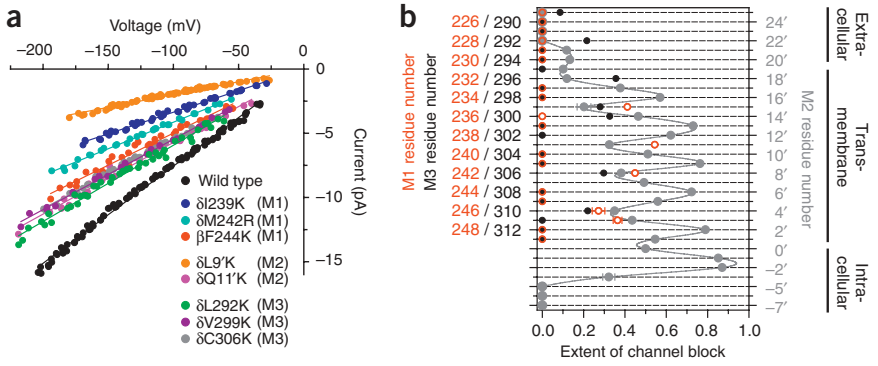

Figure 4 Extent of channel block. (**a**) Current-voltage (*I-V*) relationships for some M1 and M3 mutants and for the wild-type AChR. For clarity, only the *I-V* curve corresponding to the blocked open state (that is, the 'sublevel') is shown for each mutant. Position 244 in the β1 subunit aligns with position 247 in the δ subunit. The *I-V* curves corresponding to two M2 lysine mutants[11], δL265K (9′ position, on the pore-facing stripe of M2) and δQ267K (11′ position, on the back side of M2) are also shown. To facilitate the visual comparison of slopes, the individual *I-V* curves were voltage-shifted so that they all go through the origin. (**b**) Extent-of-channel-block values calculated from the slopes of *I-V* curves for positions in and flanking M1 (open red circles) and M3 (filled black circles). For comparison, the values corresponding to δM2 (ref. 11) are also shown (filled gray circles). M1 and M3 residue numbers (in red and black, respectively) correspond to those of the δ subunit. δM1–M2 loop and δM2 positions are denoted using the prime-numbering system (the –7′ position corresponds to δPro250, whereas 25′ corresponds to δThr281; we omit the –3′ position in the δ subunit). The unbroken line is a cubic-spline interpolation. Tentative membrane boundaries are indicated. The close correspondence between these open-state findings and the closed-state structural model (**Fig. 2a**; remember that the ionizable groups project radially several ångströms out from the Cα trace) implies that only minor conformational changes are associated with gating of the AChR. For most positions, the horizontal error bars (standard errors) are smaller than the symbols. The lumen of the pore would be to the right of the plot.

Structural inferences from the open-channel block data

A comparison of **Figures 2a** and **4b**, especially of those positions that do block the currents, indicates that neither M1 nor M3 shows substantial rotation on opening. Indeed, four out of the five positions in M1 that cause channel block when mutated to lysine and/or arginine are also oriented toward the lumen of the pore in the closed-state model. The exception is position δ247, at which a lysine residue (engineered, actually, at the aligned position in the β1 subunit) blocks the currents to an extent similar to, or even higher than, the extent of block caused by a lysine at the β1 subunit position aligned with δ246. If δPhe247 were part of the α-helix, it would not point to the same side as the other four positions; therefore, our data are consistent with this position marking the beginning of the (disordered) M1–M2 loop, or with this lysine mutation inducing the local unfolding of the M1 α-helix. The case of M3 is similar to that of M1. In M3, all the positions at which basic residues block the (open-channel) currents (**Fig. 4b**) are also the positions that are closest to the long axis of the pore in the closed-state model (**Fig. 2a**). A comparison of extent-of-block values exerted by M1 and M3 also reveals that, in the open state, the helical axis of M1 must be closer to the long axis of the pore than is the helical axis of M3, much like it is in the closed state. Remarkably, whereas basic side chains on the front side of M1 block the currents roughly as much as those engineered on the lateral stripes of M2, basic side chains introduced on the front side of M3 block as much as those on the back side of M2, in agreement with the idea that neither the M1–M2 nor the M3–M2 packing interface undergoes substantial change upon AChR opening. Finally, a comparison of **Figures 2a** and **4b** sets limits on the magnitude of the putative changes in tilt angle undergone by M1, M2 and M3. For example, M2 may tilt upon opening, but only to the extent that the intracellular third of the pore remains as the region where the M2 Cα atoms of the five subunits come closest to the long axis of the pore, and that the front stripe of M2 remains closer to the pore's axis than does that of M1 or M3, at least at the level of the membrane.

Lysines at δM1 positions 231, 232, 238 and 243 do not cause detectable channel block, presumably because they are too acidic to bind protons in the assayed pH range (see below); hence, we consider that their extent-of-block values cannot be estimated. The same is the case for δM3 position 303. Lysines at δM1 positions 227 and 228 show main-level to sublevel current fluctuations, but these are pH independent and thus are probably unrelated to proton-transfer events. Not plotted in **Figure 4b** are the points corresponding to lysine substitutions at δM3 positions 282 through 288. With the exception of the mutation of δPro286, which prevented functional expression, all other 282–288 mutants show wild type–like conductances, without detectable sojourns in subconductance levels.

To determine whether the different subunits are similarly arranged in the plane of the membrane and, thus, whether results from one or two subunits can be extrapolated to the entire heteropentamer, we mutated the positions aligned with δIle239 (an M1 residue), in all five subunits to lysine. We chose this residue because it is the M1 position at which basic residues block the currents most and because the mutation is well tolerated in the four types of subunit (α1, β1, δ and ε). Whereas the extent of channel block is 0.54 (± 0.01) in the δ subunit (**Fig. 4b**), this parameter is 0.43 (± 0.01) in β1, 0.56 (±0.01) in ε and 0.45 (± 0.01) in α1 (**Fig. 5**), clearly suggesting an almost

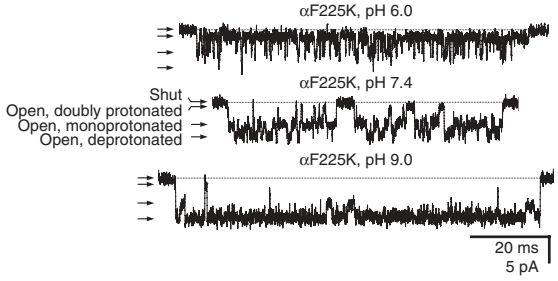

Figure 5 Two engineered lysines create two proton binding sites. Example single-channel inward currents recorded at –100 mV from a construct with a lysine at position 225 of the α1 subunit (of which the muscle-type AChR has two copies). This position aligns with positions 239 in the δ subunit (**Fig. 3a**), 236 in the β1 subunit and 234 in the ε subunit. Arrows indicate the shut (zero current) and the three open-channel current levels. The shut level of each trace is also indicated by a horizontal broken line. Display f_c = 6 kHz. [ACh] = 1 μM. The rates and pK_a values corresponding to the two proton-transfer reactions were estimated as described in **Figure 6b** and are indicated in **Table 1**. As expected from the electrostatic effect of a neighboring positive charge, the proton affinity of the monoprotonated AChR is lower than that of the deprotonated channel.

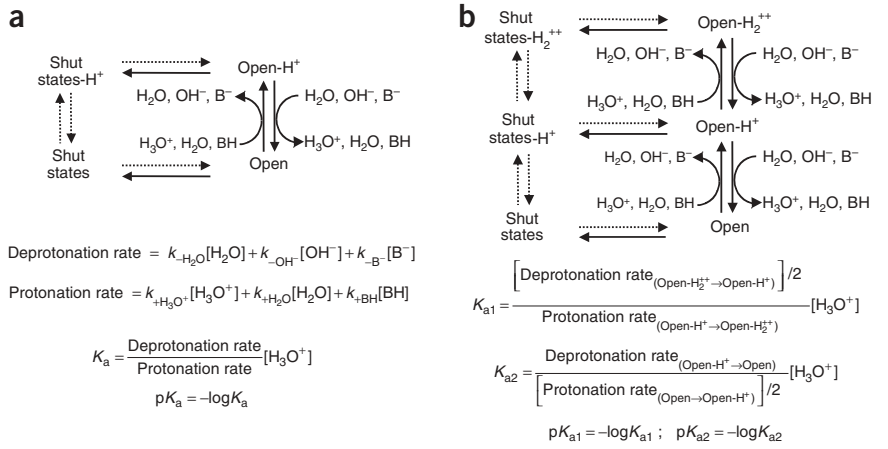

Figure 6 Experimental estimation of pK_a values using electrophysiological recordings. The AChR interconverts among closed, desensitized (both referred to, here, as 'shut states') and open conformations with or without extra protons bound to the pore domain. The association and dissociation of single protons to and from the open state (but not to and from the shut states) may manifest as discrete changes in the rate of ion flow. BH and B^- denote the protonated and deprotonated forms of the H^+ buffer, respectively. Note that the kinetics of proton transfer and channel shutting affect the dwell times in the different open-channel current levels (unbroken arrows). (**a**) Basic kinetic scheme used to estimate transition rates of mutants bearing a single engineered basic residue. (**b**) Basic kinetic scheme used in the case of the α1-subunit double-mutant constructs, which contain two lysines (one in each copy of the α1 subunit). This model assumes that both engineered lysines behave identically as far as the kinetics of proton association and dissociation are concerned and allows for interactions between them. Models that allow the two proton binding sites to be different did not yield consistent results. Rates and pK_a values in **Table 1** and **Supplementary Table 1** are expressed per protonation site; that is, they were corrected for the statistical factor.

symmetrical orientation of transmembrane segments around the central axis. This idea is further substantiated by the comparable pK_a shifts of lysines engineered at these four aligned M1 positions (**Table 1**). A similar analysis of M2 positions across subunits provides further evidence for this idea of near symmetry, especially if extent-of-block values are compared (**Supplementary Table 1** online). Hence, it seems that our use of mutants in the β1 subunit to fill the gaps left by δ-subunit positions that do not tolerate lysine or arginine mutations is amply justified.

pK_a shifts at helix-helix interfaces

Analysis of the recorded single-channel currents, now along the time axis, allowed us to investigate the M1–M2 and M3–M2 interfaces in terms of pK_a shifts. In M1, engineered lysines block the currents at only five positions, namely (in δ-subunit numbers) 235, 239, 242, 246 and 247, and their corresponding pK_a shifts relative to bulk water were estimated (**Figs. 6** and **7a**, **Table 1** and **Supplementary Fig. 2a**,**b** online). The most extracellular of these positions (δ235) and the two most intracellular ones (δ246 and δ247) show the least perturbed proton affinities, probably reflecting the penetration of water molecules from the extracellular and intracellular sides of the membrane, respectively. The stabilization afforded by these water molecules is limited, however, as evidenced by the finding that histidines engineered at these three positions (unlike lysines, histidines are well tolerated in the δ subunit) seemed to remain fully deprotonated, even at pH 5.0. The increased acidity of the imidazol group ($pK_{a,\ bulk} \cong 6.4$) in this region of M1 is fully consistent with the somewhat depressed pK_a values of lysines at these positions (**Table 1**) and a strong evidence for the notion that M1 remains shielded from the positive-charge-stabilizing central aqueous pore, upon channel opening. Indeed, histidines introduced in the pore-facing stripe of M2 exchange protons with the surrounding solvent with bulk-like or even slightly upshifted pK_a values (ref. 11). At δM1 positions 239 and 242, however, the pK_a values of lysines are more downshifted than at positions 235, 246 and 247, to the point that, at position 242, the fast kinetics of lysine deprotonation precluded the accurate estimation of the sublevel's conductance (**Fig. 3b**) and, thus, of the corresponding extent of block. This difficulty was easily overcome by mutating the δ242 residue to arginine. As expected from the known differences between these ionizable side chains in bulk water, the guanidine group of arginine is a stronger base than the lysine's amine, also in the transmembrane milieu. Notably, the microenvironment around position δ242 is hydrophobic enough to prevent the arginine's side chain from being permanently protonated (**Fig. 3b** and **Table 1**). Lysines at δM1 positions 231, 232, 238 and 243 do not attenuate the cation currents, even at pH 5.0. As positions in δM3 occupying equivalent locations in an α-helical–wheel projection do block the currents (**Fig. 7**), we rule out the possibility that these M1 positions are simply too far from the pore's axis for the electrostatic effect of the εNH_3^+ groups to reach the pore. Rather, we favor the idea that the micro-

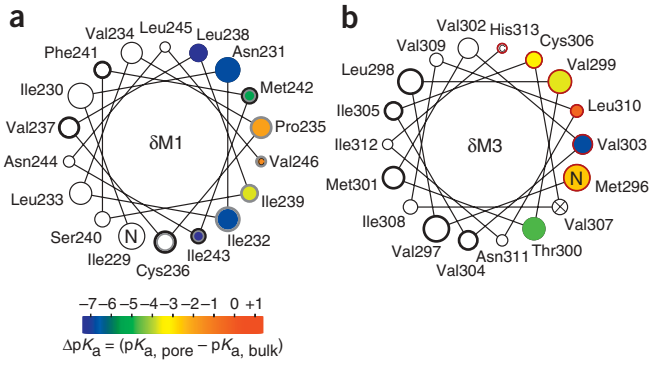

Figure 7 pK_a-shifts at protein-protein interfaces. Lysine side-chain ΔpK_a values mapped onto ideal α-helical wheel representations of 18-residue, membrane-embedded stretches of M1 (**a**) and M3 (**b**) of the δ subunit. The size of the symbols increases toward the extracellular end. Wild-type residues and the C and N termini are indicated. The color code is the same for both **a** and **b**. The lumen of the pore would be to the right of each plot. A thick black edge on the symbols identifies the positions in the α1, β1, δ and/or γ subunits of *Torpedo*'s AChR that incorporate hydrophobic photoaffinity labels in the closed state in a manner that is consistent with the label reacting from the lipid bilayer[22,48]. Symbols with a gray edge indicate the positions in M1 that lie at the interface between M1 and M2 (of the same subunit), whereas those with a maroon edge indicate the positions in M3 at the intrasubunit M3–M2 interface, as suggested by the contact plots in **Supplementary Figure 1**. The δV307K mutation in M3 prevented the expression of functional AChRs.

Table 1 Position dependence of equilibrium constants and rates of proton transfer

Mutation[a]	Aligned δ-subunit position	pH[b]	V_m (mV)[c]	Deprotonation rate (s^{-1})	Protonation rate (s^{-1})	pK_a, pore	ΔpK_a[d]	Intervals[e]	No.[f]
βP232K (M1)	235	7.4	–100	110 ± 11	3,315 ± 240	8.88 ± 0.07	–1.52	11,927	2
αF225K (M1)[g]	239	7.4	–100	924 ± 46	404 ± 62	7.03 ± 0.05	–3.37	57,122	3
αF225K (M1)[h]	239	7.4	–100	817 ± 44	677 ± 31	7.32 ± 0.03	–3.08	57,122	3
βI236K (M1)	239	7.4	–100	163 ± 21	535 ± 25	7.93 ± 0.06	–2.47	61,661	4
δI239K (M1)	-	7.4	–100	584 ± 29	278 ± 18	7.08 ± 0.04	–3.32	35,411	3
εI234K (M1)	239	7.4	–100	171 ± 6	1,245 ± 127	8.26 ± 0.04	–2.14	44,798	3
δM242K (M1)	-	6.0	–100	19,918 ± 481	3,715 ± 243	5.27 ± 0.02	–5.13	194,031	4
δM242R (M1)	-	7.4	–100	5.5 ± 0.6	15 ± 4	7.79 ± 0.09	–4.71	8,018	5
βV243K (M1)	246	7.4	–150	37 ± 3	3,339 ± 420	9.35 ± 0.04	–1.05	39,420	7
βF244K (M1)	247	7.4	–100	49 ± 5	540 ± 97	8.43 ± 0.06	–1.97	34,369	3
δM296K (M3)	-	7.4	–150	34 ± 1	225 ± 6	8.22 ± 0.01	–2.18	88,803	4
δV299K (M3)	-	7.4	–150	8.9 ± 1.5	4.7 ± 1.2	7.12 ± 0.04	–3.28	47,122	2
δT300K (M3)	-	6.0	–150	3,526 ± 162	4,403 ± 403	6.09 ± 0.04	–4.31	170,082	4
δC306K (M3)	-	7.4	–150	841 ± 28	757 ± 98	7.35 ± 0.07	–3.05	33,473	3

[a]Only mutants for which the individual rates of proton transfer could be measured are included in this table. pK_a values were also determined at other positions (see **Figure 7** and text), but these were estimated on the basis of qualitative observations. [b]Pipette-solution pH. For some of the mutants, proton-transfer events were more clearly resolved at pH 6.0 than at pH 7.4. Although pK_a values turned out to be slightly pH dependent (data not shown), the deviations from their values at pH 7.4 are expected to be small. [c]Currents were recorded at either –100 mV or –150 mV (negative inside the cell). The more hyperpolarized potential was used to facilitate the idealization of raw traces when deemed necessary. pK_a values (but not the underlying proton-transfer rates) are insensitive to the transmembrane potential. For example, at –100 mV, the pK_a of the δC306K mutant is 7.35 ± 0.09 ($n = 2$). [d]$\Delta pK_a = pK_{a,\ pore} - pK_{a,\ bulk}$. The pK_a values of the side chains of histidine, lysine and arginine in bulk water were taken from those of appropriate model compounds as 6.4 (ref. 49), 10.4 (ref. 50) and 12.5 (ref. 51), respectively. [e]Total number of idealized intervals used for kinetic analysis. [f]Number of independent patch-clamp recordings contributing to the data. Means and standard errors of proton-transfer rates and pK_as were calculated from the means of these individual recordings. [g]Both α1 subunits were mutated. The listed proton-transfer rates and pK_a correspond to the first proton-dissociation step (that is, that between the doubly protonated and the monoprotonated mutant). The two lysines were modeled as identical and were allowed to interact (see **Figure 6b**). Rates and pK_a are expressed per protonation site. [h]The listed rates and pK_a correspond to the second proton-dissociation step (that is, that between the monoprotonated and the deprotonated mutant) and are expressed per protonation site. The higher pK_a associated with this proton-transfer event compared to that between the doubly protonated and monoprotonated forms ($\Delta pK_a \cong 0.29$) reflects, at least to some extent, the electrostatic interaction between the two neighboring εNH_3^+ groups, as in any polyprotic acid-base.

environment around these positions is hydrophobic, and thus highly inhospitable for charges, explaining the large, lower-bound ΔpK_a values at these positions in **Figure 7a**. This idea is further strengthened by the finding that arginines engineered at positions δ231 and δ232 remain mostly deprotonated, even at pH 6.0 (at positions δ238 and δ243, arginine mutations resulted in a lack of functional activity). This indicates that, at δM1 positions 231 and 232, the pK_a of an arginine is clearly <5 (that is, the pK_a is reduced by >7.5 units relative to bulk water). In other words, transferring the positive charge of an arginine from bulk water into this region of the transmembrane α-helical bundle costs >10 kcal mol^{-1} (at 22 °C). Notably, recent quantum-mechanical calculations at the MP2 level of theory suggest that the pK_a of *N*-ethyl-guanidinium, an arginine side-chain model compound, is ~7 units lower in chloroform than in bulk water[21]. Together, these results emphasize the importance of a specifically tailored microenvironment (for example, cavities for water penetration, proximity to deprotonated acidic side chains and/or proximity to the membrane's polar head groups) in the case of membrane proteins that need to maintain naturally occurring arginines in nontrivial microenvironments (that is, those that are not exposed to bulk water) in the protonated state. Evidently, the AChR has not evolved to have permanently charged arginines in its hydrophobic core.

Compared to that of M1, the stripe of M3 oriented toward the pore's lumen seems better hydrated, as most pK_a values are less downshifted (**Fig. 7b**, **Table 1** and **Supplementary Fig. 2c,d**). The exception is position δ303, at which a lysine remains largely deprotonated, even at pH 6.0. This large pK_a shift firmly suggests that this portion of M3 is most tightly packed against the rest of the protein, in the open state. Notably, the nearby position δ306 is the point of closest Cα–Cα approach between M3 and M2 (of the same subunit) in the closed-state model[1] (**Supplementary Fig. 1b**), and position δ307 does not tolerate the mutation of the wild-type valine for the somewhat bulkier lysine. This is yet another suggestion that the packing interfaces change little on channel opening.

Lysines at two positions in δM3 (289 and 292, in the part of the α-helix that protrudes into the extracellular space; not plotted) also block the currents, but their pK_a values could only be estimated qualitatively. At position δ289 the pK_a is bulk-like or even somewhat upshifted, whereas at position δ292 the pK_a is lower in bulk by ~1 unit. The relatively small size of these two ΔpK_a values is consistent with the lysine pK_a shifts at most other positions at the interface between M3 and M2. For comparison, the ΔpK_a values of basic side chains engineered along M2 are shown in ref. 11.

As basic side chains on the back side and lateral stripes of M1 and M3 do not block the currents, we did not introduce ionizable amino acids along M4, the transmembrane α-helices that are both most lipid-exposed[22,23] and farthest from the long axis of the pore (**Fig. 1b**). Thus, although the breaking and formation of interhelical contacts involving M4 residues probably contribute to the overall energetics of AChR gating (for example, ref. 24) we cannot offer any insight as to the magnitude of the reorganization of the M4–M1 or M4–M3 packing interfaces upon channel opening.

DISCUSSION

Having placed limits on the extent of rotation and the change in tilt angle, and on the degree to which the AChR packing interfaces reorganize upon opening, it could still be argued that our results cannot rule out a large displacement of M1, M2 and M3 as a unit, parallel to the plane of the membrane and away from the pore's long axis. Indeed, as we do not know the exact mathematical relationship between the extent of channel block and the (absolute) distance from the engineered ionizable groups to the long axis of the pore, such displacement could, in principle, be arbitrarily large. However, it is important to bear in mind that the narrowest constriction of the muscle-type AChR in the open state (that is, the 'selectivity filter' region, formed by the cytoplasmic ends of the five M2 α-helices) has from permeability-ratio measurements been inferred to have a diameter in the 7.2–8.4 Å range[25,26], whereas the diameter of this same

region of the channel in the closed-state structural model[1] can be estimated to be ~6–8 Å (depending on the method used to measure it)[27,28]. Hence, despite the limited resolution of the cryo-EM data and the indirect nature of the structural information inferred from functional studies, it is clear that the uniform widening of the AChR's pore domain, parallel to the membrane, cannot be greater than a few ångströms.

A trivial interpretation of our results would be that the imaged structure[1,6] represents the open, not the closed, conformation of the AChR. This possibility seems unlikely, however, because the cryo-EM images were obtained in the absence of agonist and because various molecular simulation approaches have assigned a negligible conductance to the derived structural model[29,30]. Instead, we favor the idea that the differences between the closed and open conformations of the AChR's pore are much more subtle than previously envisaged and too small to be described in detail by our approach. Notably, however, the idea of a small dilation of the pore, one that does not require large contortions of the protein to be realized, is fully consistent with the concept of hydrophobic gating[6,31,32]; that is, the notion of a desolvation barrier, as opposed to a steric one, acting as the channel's activation gate.

Theoretical approaches have suggested that the permeability of model hydrophobic nanopores to water and ions is a nearly all-or-nothing, steep function of the lumen's diameter[32–35]. Similarly, in the case of the AChR, simulations have suggested that increasing the radius of the hydrophobic, narrowest portion of the closed-state pore by as little as ~1.5 Å is sufficient to increase the computed conductance to values that are close to those observed experimentally for the open channel[30]. Gratifyingly, this finding is in close agreement with the results of comparable simulations on other ion channels that also (presumably) have desolvation barriers acting as gates (for example, refs. 36,37). The idea of a limited rearrangement of the pore domain upon AChR gating that emerges from the comparison of our open-state experimental data and the closed-state structural model[1] is certainly consistent with these theoretical predictions, and hence suggests that the AChR has evolved to fully exploit the ion- and water-conduction properties of nonpolar subnanometer pores. On gating, the diameter of the gate region would fluctuate between two values directly flanking this narrow, sharp-transition zone: an even narrower constriction in the closed state would not make the channel shut any more tightly, nor would a wider opening in the open state make the channel conduct ions any faster. The kinetics of gating of the wild-type muscle-type AChR are so precisely tuned for fast and reliable synaptic transmission that more extensive rearrangements, which would be likely to lead to slower gating rate constants, would be disadvantageous.

The proposed limited rearrangement of membrane-embedded α-helices upon AChR gating contrasts markedly with the much larger reorganization of transmembrane protein-protein and protein-lipid contacts proposed to underlie, for example, the resting-to-activated conformational change in voltage-dependent K^+ channels. Indeed, a recent model[38] postulates that, on membrane depolarization, both the S3 and S4 transmembrane segments of Shaker K^+ channels undergo large displacements relative to the rest of the protein and with respect to one another, with the arginine-containing S4 segments rotating ~180° as they move outward by 6–8 Å.

Remarkably, the AChR tolerates the introduction of lysines at most positions of the mutated protein-protein and protein-lipid interfaces, giving rise to functional ACh-gated channels. Rather than keeping the proton bound and inducing the local unfolding of the protein that would be needed to solvate the positive charge properly, the introduced lysines lower their pK_a values so that they can lose the proton and become neutral, at least part of the time. A similar behavior was observed for the engineered arginines. Although our data set for this amino acid is less extensive than that for lysines, we have presented clear examples here of transmembrane positions at which the guanidinium group becomes so acidic that it is not permanently charged.

Note added in proof: While this manuscript was in press, the crystal structure (3.3-Å resolution) of a pentameric ligand-gated ion channel from the bacterium *Erwinia chrysanthemi* (ELIC; 16% sequence identity to the α1 AChR subunit from *Torpedo marmorata*) in a nonconductive conformation was published (PDB 2VL0)[52]. Quantitative comparison of our mouse muscle open-channel data with the ELIC structure strongly supports the idea of small rearrangements upon channel opening that we have inferred through comparison with the 4.0-Å resolution cryo-EM model of a muscle-type AChR from *T. marmorata* determined in the absence of activating ligands (PDB 2BG9). As for muscle-type AChR, the rotation of M1, M2 and M3 in ELIC upon channel opening would be minimal, but the outward tilting of the extracellular ends of M2 and M3 would be more pronounced. The physically occluded extracellular portion of the transmembrane pore of ELIC may well reflect a more stable closed-channel conformation compared to that of the muscle-type AChR and may be an indirect result of the lack of the intracellular domain and/or of the different pore-lining side chains.

METHODS

General procedures. HEK-293 cells were transiently transfected with mouse muscle adult-type AChR complementary DNAs. Mutations were engineered using the QuikChange site-directed mutagenesis kit (Stratagene) and were confirmed by dideoxy sequencing. We chose (here and previously[11]) the δ subunit as our target for the extensive scanning mutagenesis, simply because it is one of the subunits that is present as a single copy in the heteropentameric ($(\alpha1)_2\beta1\delta\varepsilon$) complex (**Fig. 1b**); this considerably simplified the analysis of the data. The muscle AChR is unique among cysteine-loop receptors in that its subunit stoichiometry is relatively invariant, a fundamental advantage for this type of study. Indeed, we have never observed the incorporation of an unexpected number of mutant subunits into the receptor (which would be easily detected in the current recordings—compare **Fig. 3** with **Fig. 5**), nor have our attempts to express 'δ-less' AChRs (by omitting the cDNA encoding for the δ subunit from the transfection mixture) resulted in typical levels of AChR activity. Single-channel patch-clamp currents were recorded in the cell-attached configuration at 22 °C. The bath solution contained 142 mM KCl, 5.4 mM NaCl, 1.8 mM $CaCl_2$, 1.7 mM $MgCl_2$ and 10 mM HEPES-KOH buffer (pH 7.4). The pipette solution was identical to that in the bath with the exception of the H^+ buffer, which varied depending on the desired pH of the solution. These buffers were acetic acid/acetate (pH 5.0), MES (pH 6.0), HEPES (pH 7.4) or *N*-tris[hydroxymethyl]methyl-4-aminobutane-sulfonic acid (TABS; pH 9.0), all titrated to a final pH with KOH. The pipette solution also contained 1 μM ACh. Single-channel currents were digitized at 100 kHz, filtered (cascaded $fc \cong 30$ kHz) and idealized (using the SKM algorithm in QuB software[39]) to obtain the corresponding current amplitudes and dwell-time series.

Experimental estimation of the extent of channel block. The extent of channel block for each construct was calculated as the difference between the conductance values of the main level and the sublevel (estimated from plots similar to those in **Fig. 4a**) normalized by the conductance of the main level. The standard errors of these conductance estimates were used to calculate the standard errors of the extent-of-block values.

Experimental estimation of pK_a values. Protonation and deprotonation rates (and all other transition rates) were estimated from maximum-likelihood fits of dwell-time series with kinetic models based on those in **Figure 6**. Additional shut states were added to these models (connected to the existing shut states) until the Schwarz criterion[40] for best fit was satisfied. To this end, we used the MIL algorithm in QuB software[41] with a retrospectively imposed time resolution of 25–50 μs. The ratio between the proton-dissociation and

proton-association rates thus estimated gives the ratio of the probabilities of the engineered ionizable side chain being deprotonated versus protonated while the channel is open. The reported pK_a values (**Fig. 7**, **Table 1** and **Supplementary Table 1**) were calculated from the product of these ratios and the concentration of hydronium ions in the pipette's solution (**Fig. 6**). To increase the number of proton-transfer events occurring while the channel is open, mutations that prolong individual activations of the channel were also introduced in the studied constructs. These mutations were one, or a combination of αS269I (ref. 42), βV266M (ref. 43), δS268Q (ref. 44), δS268N (ref. 44) or εT264P (ref. 45).

Note: Supplementary information is available on the Nature Structural & Molecular Biology website.

ACKNOWLEDGMENTS

We thank S. Sine (Mayo Clinic College of Medicine, Rochester, Minnesota, USA) for the wild-type muscle AChR subunit cDNA; G. Westfield and J. Gasser for technical assistance; and E. Tajkhorshid, M. Sotomayor, S. Varma and F.D. González-Nilo for advice and discussions. This work was supported by a grant from the US National Institutes of Health (R01-NS042169 to C.G.).

AUTHOR CONTRIBUTIONS

G.D.C. designed and performed the experiments, and analyzed data; C.G. designed experiments, analyzed data and wrote the manuscript.

Published online at http://www.nature.com/nsmb/
Reprints and permissions information is available online at http://npg.nature.com/reprintsandpermissions

1. Unwin, N. Refined structure of the nicotinic acetylcholine receptor at 4 Å resolution. *J. Mol. Biol.* **346**, 967–989 (2005).
2. Dilger, J.P. & Liu, Y. Desensitization of acetylcholine receptors in BC3H–1 cells. *Pflugers Arch.* **420**, 479–485 (1992).
3. Unwin, N. Acetylcholine receptor channel imaged in the open state. *Nature* **373**, 37–43 (1995).
4. Arévalo, E., Chiara, D.C., Forman, S.A., Cohen, J.B. & Miller, K.W. Gating-enhanced accessibility of hydrophobic sites within the transmembrane region of the nicotinic acetylcholine receptor's δ-subunit. A time-resolved photolabeling study. *J. Biol. Chem.* **280**, 13631–13640 (2005).
5. Sansom, M.S.P. Twist to open. *Curr. Biol.* **5**, 373–375 (1995).
6. Miyazawa, A., Fujiyoshi, Y. & Unwin, N. Structure and gating mechanism of the acetylcholine receptor pore. *Nature* **423**, 949–955 (2003).
7. Law, R.J., Henchman, R.H. & McCammon, J.A. A gating mechanism proposed from a simulation of a human α7 nicotinic acetylcholine receptor. *Proc. Natl. Acad. Sci. USA* **102**, 6813–6818 (2005).
8. Paas, Y. *et al.* Pore conformations and gating mechanism of a Cys-loop receptor. *Proc. Natl. Acad. Sci. USA* **102**, 15877–15882 (2005).
9. Cheng, X., Ivanov, I., Wang, H., Sine, S.M. & McCammon, J.A. Nanosecond time scale conformational dynamics of the human α7 nicotinic acetylcholine receptor. *Biophys. J.* **93**, 2622–2634 (2007).
10. Cheng, X., Wang, H., Grant, B., Sine, S.M. & McCammon, J.A. Targeted molecular dynamics study of C-loop closure and channel gating in nicotinic receptors. *PLOS Comput. Biol.* **2**, e134 (2006).
11. Cymes, G.D., Ni, Y. & Grosman, C. Probing ion-channel pores one proton at a time. *Nature* **438**, 975–980 (2005).
12. Warshel, A. Calculations of enzymatic reactions: calculations of pK_a, proton transfer reactions, and general catalysis reactions in enzymes. *Biochemistry* **20**, 3167–3177 (1981).
13. Dao-Pin, S., Anderson, D.E., Baase, W.A., Dahlquist, F.W. & Matthews, B.W. Structural and thermodynamic consequences of burying a charged residue within the hydrophobic core of T4 lysozyme. *Biochemistry* **30**, 11521–11529 (1991).
14. Schutz, C.N. & Warshel, A. What are the dielectric "constants" of proteins and how to validate electrostatic models? *Proteins* **44**, 400–417 (2001).
15. Fitch, C.A. *et al.* pK_a values of buried residues: analysis with continuum methods and role of water penetration. *Biophys. J.* **82**, 3289–3304 (2002).
16. Mehler, E.L., Fuxreiter, M., Simon, I. & García-Moreno, E.B. The role of hydrophobic microenvironments in modulating pK_a shifts in proteins. *Proteins* **48**, 283–292 (2002).
17. Guillén Schlippe, Y.V. & Hedstrom, L. A twisted base? The role of arginine in enzyme-catalyzed proton abstractions. *Arch. Biochem. Biophys.* **433**, 266–278 (2005).
18. Kim, J., Mao, J. & Gunner, M.R. Are acidic and basic groups in buried proteins predicted to be ionized? *J. Mol. Biol.* **348**, 1283–1298 (2005).
19. Niemeyer, M.I. *et al.* Neutralization of a single arginine residue gates open a two-pore domain, alkali-activated K^+ channel. *Proc. Natl. Acad. Sci. USA* **104**, 666–671 (2007).
20. Jansen, M. & Akabas, M.H. State-dependent cross-linking of the M2 and M3 segments: functional basis for the alignment of $GABA_A$ and acetylcholine receptor M3 segments. *J. Neurosci.* **26**, 4492–4499 (2006).
21. Norberg, J., Foloppe, N. & Nilsson, L. Intrinsic relative stabilities of the neutral tautomers of arginine side-chain models. *J. Chem. Theory Comput.* **1**, 986–993 (2005).
22. Blanton, M.P. & Cohen, J.B. Identifying the lipid-protein interface of the *Torpedo* nicotinic acetylcholine receptor: secondary structure implications. *Biochemistry* **33**, 2859–2872 (1994).
23. Hamouda, A.K., Chiara, D.C., Sauls, D., Cohen, J.B. & Blanton, M.P. Cholesterol interacts with transmembrane α-helices M1, M3, and M4 of the *Torpedo* nicotinic acetylcholine receptor: photolabeling studies using [^{3}H]azicholesterol. *Biochemistry* **45**, 976–986 (2006).
24. Tamamizu, S. *et al.* Functional effects of periodic tryptophan substitutions in the α M4 transmembrane domain of the *Torpedo californica* nicotinic acetylcholine receptor. *Biochemistry* **39**, 4666–4673 (2000).
25. Dwyer, T.M., Adams, D.J. & Hille, B. The permeability of the endplate channel to organic cations in frog muscle. *J. Gen. Physiol.* **75**, 469–492 (1980).
26. Cohen, B.N., Labarca, C., Davidson, N. & Lester, H.A. Mutations in M2 alter the selectivity of the mouse nicotinic acetylcholine receptor for organic and alkali metal cations. *J. Gen. Physiol.* **100**, 373–400 (1992).
27. Smart, O.S., Neduvelil, J.G., Wang, X., Wallace, B.A. & Sansom, M.S.P. HOLE: a program for the analysis of the pore dimensions of ion channel structural models. *J. Mol. Graph.* **14**, 354–360 (1996).
28. Varma, S., Chiu, S.W. & Jakobsson, E. The influence of amino acid protonation states on molecular dynamics simulations of the bacterial porin OmpF. *Biophys. J.* **90**, 112–123 (2006).
29. Beckstein, O. & Sansom, M.S.P. A hydrophobic gate in an ion channel: the closed state of the nicotinic acetylcholine receptor. *Phys. Biol.* **3**, 147–159 (2006).
30. Corry, B. An energy-efficient gating mechanism in the acetylcholine receptor channel suggested by molecular and Brownian dynamics. *Biophys. J.* **90**, 799–810 (2006).
31. White, B.H. & Cohen, J.B. Agonist-induced changes in the structure of the acetylcholine receptor M2 regions revealed by photoincorporation of an uncharged nicotinic noncompetitive antagonist. *J. Biol. Chem.* **267**, 15770–15783 (1992).
32. Beckstein, O., Biggin, P.C. & Sansom, M.S.P. A hydrophobic gating mechanism for nanopores. *J. Phys. Chem. B* **105**, 12902–12905 (2001).
33. Lynden-Bell, R.M. & Rasaiah, J.C. Mobility and solvation of ions in channels. *J. Chem. Phys.* **105**, 9266–9280 (1996).
34. Beckstein, O. & Sansom, M.S.P. The influence of geometry, surface character, and flexibility on the permeation of ions and water through biological pores. *Phys. Biol.* **1**, 42–52 (2004).
35. Peter, C. & Hummer, G. Ion transport through membrane-spanning nanopores studied by molecular dynamics simulations and continuum electrostatics calculations. *Biophys. J.* **89**, 2222–2234 (2005).
36. Sotomayor, M., van der Straaten, T.A., Ravaioli, U. & Schulten, K. Electrostatic properties of the mechanosensitive channel of small conductance MscS. *Biophys. J.* **90**, 3496–3510 (2006).
37. Vora, T., Corry, B. & Chung, S.H. Brownian dynamics investigation into the conductance state of the MscS channel crystal structure. *Biochim. Biophys. Acta* **1758**, 730–737 (2006).
38. Pathak, M.M. *et al.* Closing in on the resting state of the Shaker K^+ channel. *Neuron* **56**, 124–140 (2007).
39. Qin, F. Restoration of single-channel currents using the segmental k-means method based on hidden Markov modeling. *Biophys. J.* **86**, 1488–1501 (2004).
40. Schwarz, G. Estimating the dimension of a model. *Ann. Statist.* **6**, 461–464 (1978).
41. Qin, F., Auerbach, A. & Sachs, F. Estimating single-channel kinetic parameters from idealized patch-clamp data containing missed events. *Biophys. J.* **70**, 264–280 (1996).
42. Grosman, C., Salamone, F.N., Sine, S.M. & Auerbach, A. The extracellular linker of muscle acetylcholine receptor channels is a gating control element. *J. Gen. Physiol.* **116**, 327–339 (2000).
43. Engel, A.G. *et al.* New mutations in acetylcholine receptor subunit genes reveal heterogeneity in the slow-channel congenital myasthenic syndrome. *Hum. Mol. Genet.* **5**, 1217–1227 (1996).
44. Grosman, C. & Auerbach, A. Asymmetric and independent contribution of the second transmembrane segment 12′ residues to diliganded gating of acetylcholine receptor channels. A single-channel study with choline as the agonist. *J. Gen. Physiol.* **115**, 637–651 (2000).
45. Ohno, K. *et al.* Congenital myasthenic syndrome caused by prolonged acetylcholine receptor channel openings due to a mutation in the M2 domain of the ε subunit. *Proc. Natl. Acad. Sci. USA* **92**, 758–762 (1995).
46. Humphrey, W., Dalke, A. & Schulten, K. VMD: visual molecular dynamics. *J. Mol. Graph.* **14**, 33–38 (1996).
47. Frishman, D. & Argos, P. Knowledge-based protein secondary structure assignment. *Proteins* **23**, 566–579 (1995).
48. Blanton, M.P., McCardy, E.A., Huggins, A. & Parikh, D. Probing the structure of the nicotinic acetylcholine receptor with the hydrophobic photoreactive probes [^{125}I]TIDBE and [^{125}I]TIDPC/16. *Biochemistry* **37**, 14545–14555 (1998).
49. Tanokura, M. ^{1}H-NMR study on the tautomerism of the imidazole ring of histidine residues. I. Microscopic p*K* values and molar ratios of tautomers in histidine-containing peptides. *Biochim. Biophys. Acta* **742**, 576–585 (1983).
50. Thurlkill, R.L., Grimsley, G.R., Scholtz, J.M. & Pace, C.N. p*K* values of the ionizable groups of proteins. *Protein Sci.* **15**, 1214–1218 (2006).
51. Warwicker, J. Improved pK_a calculations through flexibility based sampling of a water-dominated interaction scheme. *Protein Sci.* **13**, 2793–2805 (2004).
52. Hilf, R.J.C. & Dutzler, R. X-ray structure of a prokaryotic pentameric ligand-gated ion channel. *Nature* advance online publication, doi:10.1038/nature06717 (5 March 2008).